# Flow Physics Analysis of Three-Bucket Helical Savonius Rotor at $90^0$ Twist Angle Using CFD

## Pinku Debnath, [1] Rajat Gupta[2]

[12]*Mechanical Engineering, / National Institute of Technology, Silchar, India*

**Abstract:** *In this research work the flow behavior was analyzed, which affect the power coefficient as well as torque coefficient of a helical Savonius rotor is investigated by means of commercial code CFD. Conventional three bladed Savonius rotors have high coefficient of static torque at certain rotor angles and negative coefficient of static torque at certain rotor angle. In order to increase the efficiency of all rotor angles the system a helical Savonius rotor with a twist of certain proposed degree is introduced. A three-dimensional model of $90^0$ twist three blades helical Savonius rotor at $0^0$, $60^0$, $120^0$ and $150^0$ rotor angle has been constructed by using the software gambit of the Fluent 6.3 package. The contours of static pressure and velocity magnitude around the rotor blades area at horizontal iso-plane is obtained from the CFD simulation. High performance was obtained at advanced bucket in upstream air flow at $60^0$ rotor angle and maximum positive static pressure obtained at $150^0$ rotor angle, which affect the positive coefficient of static torque.*

**Keywords:** *Helical Savonius rotor, rotor angle, CFD analysis, velocity contour, and static pressure contour.*

## I. INTRODUCTION

The Savonius rotor is a vertical axis wind turbine (VAWT) originally invented by a Finnish engineer Sigurd J. Savonius in 1922 [1]. N. Fulisawa observed the relation between rotor performance and flow characteristics field around a Savonius rotor by using a laser light sheet and a CCD camera with a shutter speed of 0.002s [2]. Nobuyuki Fujisawa measured the flow fields in an around Savonius rotors at various overlap ratios with particle imaging velocimetry technology and comparison analysis is conducted between a vertical-axis spiral rotor and a conventional Savonius rotor by using CFD technology [3]. The flow field around a Savonius rotor, which is closely related to the torque and the power performance of the rotor, has been investigated by many researchers to clarify the power mechanism of the rotor. Most investigations have been experimental studies with flow visualization techniques, such as tufts [4, 5]. The flow physics of the rotor with overlap variation 12.37% to 25.87% were analysed with the help of velocity and pressure contours of the rotor. From this analysis the overlap of 19.87% was the optimum overlap condition at which pressure and velocity differences across the rotor were the highest for which maximum power extraction by the rotor would be possible at that overlap condition [6]. The combination of Darrieus and Savonius rotors thus exhibits high starting torque and high power coefficient. Keeping the above points they have made to study the flow physics of a combined three-bucket Darrieus and Savonius rotor using Fluent 6.0. They have considered four overlap conditions between 10.87% to 25.87% for the Savonius part of the combined rotor and observed highest relative speed and highest pressure of the combined rotor near its top at 15.37% overlap condition [7]. M.A.Kamoji et al. [8] performed the static torque coefficients at all the rotor angles for helical Savonius rotors are positive. However, for conventional Savonius rotor, there are several rotor angles at which static torque coefficient is negative. Conventional Savonius rotor configurations with steady two-dimensional RANS CFD simulations were also conducted by Gupta et al. in which static torque predictions for a Savonius rotor with external flow Control demonstrated good agreement with the corresponding experimental wind tunnel results [9]. Gupta et al. [10] has also been observed that the aerodynamic performance and optimum overlap of the combined rotor are strongly controlled by the flow physics of the individual rotors. Katsuya I et al. [11] simulated numerically the flow over a two-bucket Savonius rotor by solving 2D finite volume equations using an upwind scheme for unstructured mesh. The result shows good matching with the experimental values of power coefficient, aerodynamic coefficients. M., Manzoor Hussain, Mehdi et al. [12] conducted the enhancement of efficiency by modifying the blades configuration from straight semicircular to a twisted semi circular one. Wind flow analysis was done over each configuration of the rotor with the blade twist ranging from $5^0$ to $60^0$ in a steps of $5^0$. Maximum efficiency is obtained 33.85% at $45^0$ twist angle, when compared to 25.6% without twist. A fully automatic optimization finally takes place, the commercial tool Gambit for geometry and grid generation (including quality check) and the industrial CFD code ANSYS-Fluent to compute the flow field around the Savonius rotor [13].

## II. DESCRIPTION OF PHYSICAL MODEL

In the present research work, the performance of a three-bucket helical Savonius rotor with semicircular profiles buckets at 90° twist angle as shown in Figure- 1 was analyzed. The operation of the rotor is simulated with the variation in rotor angle at $0^0$, $60^0$, $120^0$ and $150^0$. The diameter of the rotor has a value of 24cm, while the value of the rotor height is 40cm. The thickness of the buckets is 3 mm.

## III.   DETAILS OF COMPUTATIONAL DOMAIN

The three dimensional computational domain of three-bladed helical Savonius rotor along with the boundary conditions is shown in the Figure- 2. The computational domain resembles was 60cm x 60cm in cross-section. Wind speed was considered on the inlet face ABCD, outflow was considered on the outlet face EFGH, symmetry condition was considered for the side walls of the computational domain and blades are consider as rotating wall. The computational domain was adopted of the unstructured hexahedral mesh and the moving mesh techniques in Figure- 3. The computations were initially carried out with various levels of refinement of mesh which is done in gambit of the Fluent 6.3 package. The number of cells and nodes involved in meshing of the rotor with various levels are given in Table 1. The grid independent limit computational mesh (Masson eta al., 1997) [14] was obtained by changing the resolution of mesh at all important areas of the rotor which is shown in the Figure- 4.

### 3.1 Computational Domain Discretization Method:

The continuity equation, Newton's second law, the conservation of momentum equation (N-S equation) and realizable k-ε turbulence model are numerically solved by the commercial software FLUENT 6.3. Finite Volume Method is used for discretizing a differential equation and computes the static pressure and velocity fields of the flow on the rotor buckets. Applying the discretizing techniques the computational domain divided into a finite number of elementary control volumes. The sequential algorithm, Semi-Implicit Method for Pressure-Linked Equation (SIMPLE), was used for solving all the scalar variables with the k-ε turbulence model. The finite volume discretization transforms the differential equations governing the flow in a linear system of algebraic equations that is iteratively solved.

### 3.2 Mathematical Formulation:

In the present study, the results were obtained by applying the Finite Volume Method to solve the conservation equations of the turbulent air flow on the helical Savonius rotor, which allows the calculation of the performance of the rotor. Among these conservation equations, there is the mass balance equation. The Eq. (1) with indicial notation represents the mass balance, where ρ is the density, $\vec{V}$ is the velocity vector and value of $\vec{S}_m$ is zero for steady-state flow.

$$\frac{\partial \rho}{\partial t} + \nabla . (\rho \vec{V}) = \vec{S}_m = 0 \tag{1}$$

The momentum equation must be solved along with the mass balance equation. The Eq. (2) represents the momentum equation, where $\rho$ is the density, $\vec{V}$ is the velocity vector, p is the static pressure, and $\bar{\bar{\tau}}$ is the stress tensor (described below), and $\rho\vec{g}$ and $\vec{F}$ are the gravitational body force and external body forces (e.g., that arise from interaction with the dispersed phase), respectively.

$$\frac{\partial}{\partial t} (\rho \vec{V}) + \nabla . (\rho \vec{V} \vec{V}) = -\nabla p + \nabla . \bar{\bar{\tau}} + \rho \vec{g} + \vec{F} \tag{2}$$

The stress tensor is given by

$$\bar{\bar{\tau}} = \mu [(\nabla . \vec{V} + \nabla . \vec{V}^T) - \frac{2}{3}\nabla . \vec{V} I] \tag{3}$$

Where μ is the molecular viscosity, I is the unit tensor, and the second term on the right hand side is the effect of volume dilation.

### 3.3 Turbulence Model:

The realizable k-ε turbulence model provides superior performance for flows involving rotation, boundary layers under strong adverse pressure gradients, separation, and recirculation. The modeled transport equations for k and ε in the realizable k-ε model are:

$$\frac{\partial(\rho k)}{\partial t} + \frac{\partial(\rho k u_j)}{\partial x_j} = \frac{\partial}{\partial x_j}[(\mu + \frac{\mu_t}{\sigma_k})\frac{\partial k}{\partial x_j}] + G_k + G_b - \rho_\varepsilon - Y_M + S_k \tag{4}$$

and

$$\frac{\partial(\rho \varepsilon)}{\partial t} + \frac{\partial(\rho \varepsilon u_i)}{\partial x_i} = \frac{\partial}{\partial x_j}[(\mu + \frac{\mu_t}{\sigma_\varepsilon})\frac{\partial \varepsilon}{\partial x_j}] + \rho C_1 S_\varepsilon - \rho C_2 \frac{\varepsilon^2}{k + \sqrt{v\varepsilon}} + C_{1\varepsilon}\frac{\varepsilon}{k} C_{3\varepsilon} G_b + S_\varepsilon \tag{5}$$

Where

$$C_1 = \max\left[0.43.\frac{\eta}{\eta+5}\right], \qquad \eta = S.\frac{k}{\varepsilon} \quad \text{and} \quad S = \sqrt{2S_{ij}S_{ij}}$$

In these equations, $G_k$ represents the generation of turbulence kinetic energy due to the mean velocity gradients. $G_b$ is the generation of turbulence kinetic energy due to buoyancy. $Y_M$ represents the contribution of the fluctuating dilatation in compressible turbulence to the overall dissipation rate. $C_2$ And $C_{1\varepsilon}$ are constants. $\sigma_k$ and $\sigma_\varepsilon$ are the turbulent Prandtl numbers for $k$ and $\varepsilon$, respectively $S_k$ and $S_\varepsilon$ are user-defined source terms [15].

## IV.  FIGURES AND TABLES
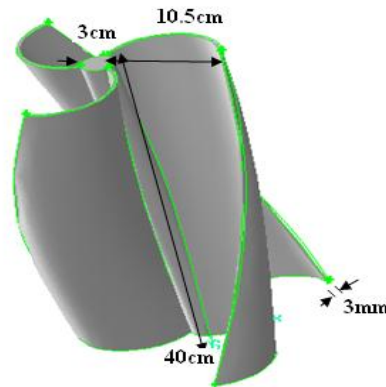


**Figure 1: Physical model of 90° twist three bucket helical Savonius rotor**
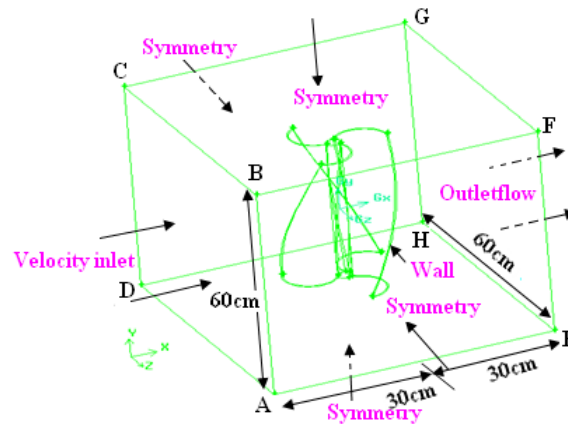


**Figure 2: Computational domain and boundary condition**
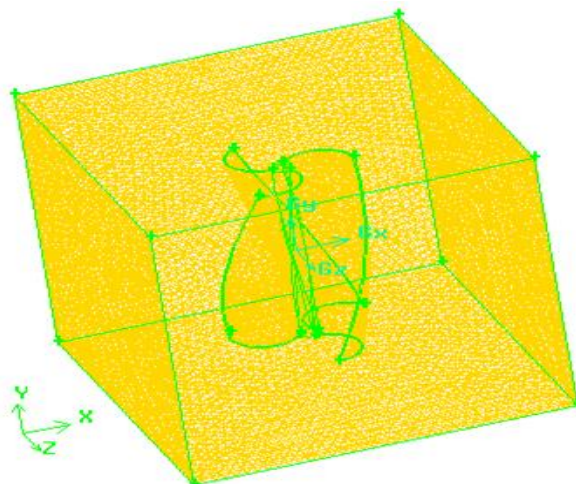


**Figure 3: Computational mesh of 90° twist helical Savonius rotor**

**Table 1: Details of refinement levels of the 3-buckets helical Savonius rotor**

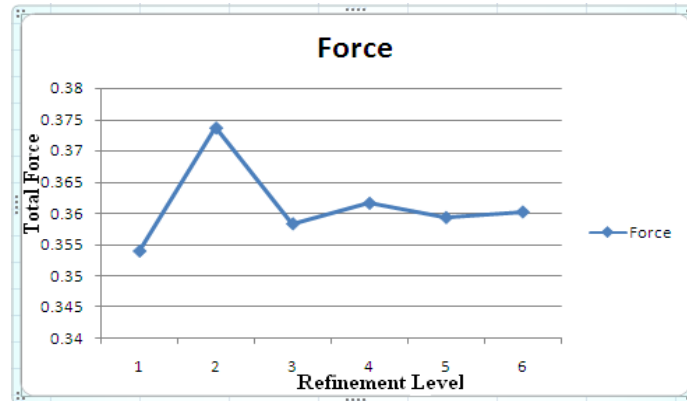| Refinement Level | No. of Nodes | No. of Elements |
|---|---|---|
| 1 | 34226 | 179994 |
| 2 | 35619 | 188283 |
| 3 | 37039 | 195053 |
| 4 | 44244 | 215022 |
| 5 | 48459 | 258595 |
| 6 | 50430 | 267086 |



**Figure 4: Variation of total force with respect to refinement level**

## V. RESULTS AND DISCUSSION
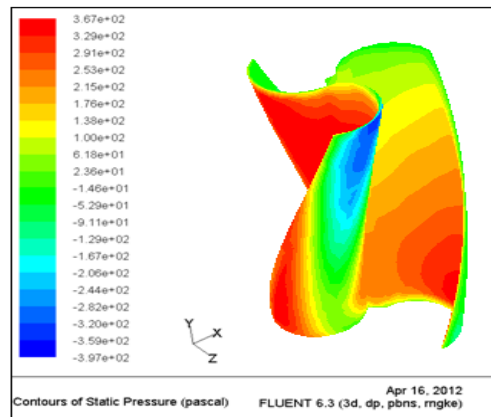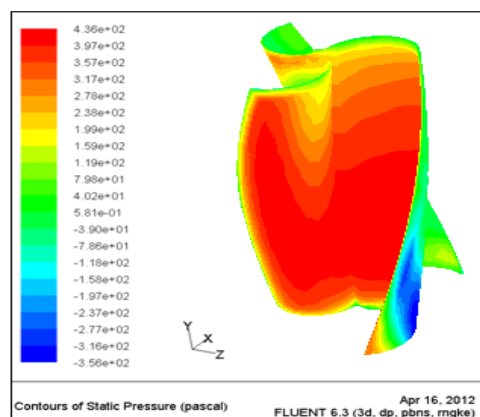


**Figure 4(a): Static pressure magnitude contour for $0^0$ rotor angle**
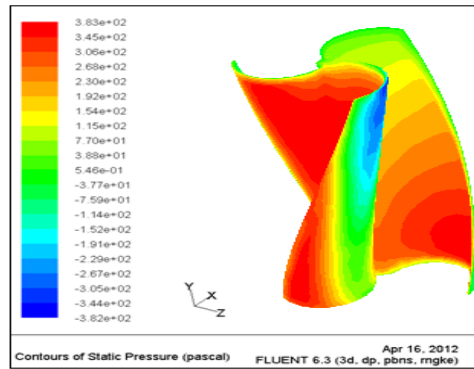


**Figure 4(b): Static pressure magnitude contour for $60^0$ rotor angle**

**Figure 4(c): Static pressure magnitude contour for $120^0$ rotor angle**
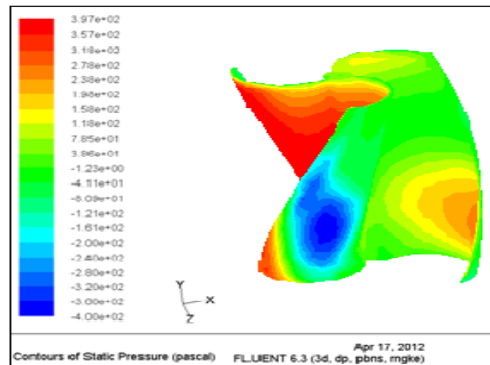


**Figure 4(d): Static pressure magnitude contour for $150^0$ rotor angle**

The helical Savonius rotor with three bladed $90^0$ twist angle, the contour plot analysis at $0^0$, $60^0$, $120^0$ and $150^0$ rotor angle for one revolution of the rotor, the contour plot analysis gives an idea about the flow physics of a wind rotor and its power generation mechanism. In the present study, relative velocity magnitude (velocity of the rotor relative to wind) and static pressure contours are analyzed. Fig- 5(a) to Fig- 5(d) show the velocity contours of the three-bucket helical Savonius rotor for different rotor angle conditions of $0^0$, $60^0$, $120^0$ and $150^0$. The velocity magnitude contour shows that the maximum velocity magnitudes near the chord end of advance bucket and decrease downstream side of the rotor. For $0^0$ rotor angle velocity obtained $2.98\times10^1$ m/sec to 1.49m/sec, for $60^0$ rotor angle $2.86\times10^1$ m/sec to 1.43m/sec, for $120^0$ rotor angle $2.98\times10^1$ m/sec to 1.49m/sec and at $150^0$ rotor angle $2.95\times10^1$ m/sec to 1.47m/sec at XZ iso-plane. Fig- 4 (a) to Fig- 4 (d) show the static pressure flow separation near to the bucket wall and Fig- 6 (a) to Fig- 6 (d) show the static pressure contours of the rotor for the aforesaid rotor angle conditions. These pressure contours show a decrease of static pressure from the upstream side to the downstream side across the rotor, which results in useful for evaluate the performance of rotor. At $0^0$ rotor angle Fig- 6(a), static pressure decreases from $3.67\times10^2$ Pascal to $-3.97\times10^2$ Pascal from upstream side to downstream side. At $60^0$ rotor angle Fig- 6(b), static pressure decreases from $4.36\times10^2$ Pascal to $-3.56\times10^2$ Pascal from upstream side to downstream side. At $120^0$ rotor angle Fig- 6(c), static pressure decreases from $3.83\times10^2$ Pascal to $-3.82\times10^2$ Pascal from advanced bucket to downstream bucket. At $150^0$ rotor angle Fig- 6(d), static pressure decreases from $3.97\times10^2$ Pascal to $-4.004\times10^2$ Pascal from upstream bucket to downstream bucket at XZ iso-plane.
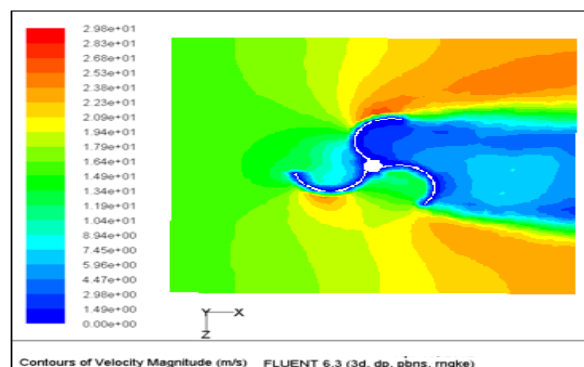


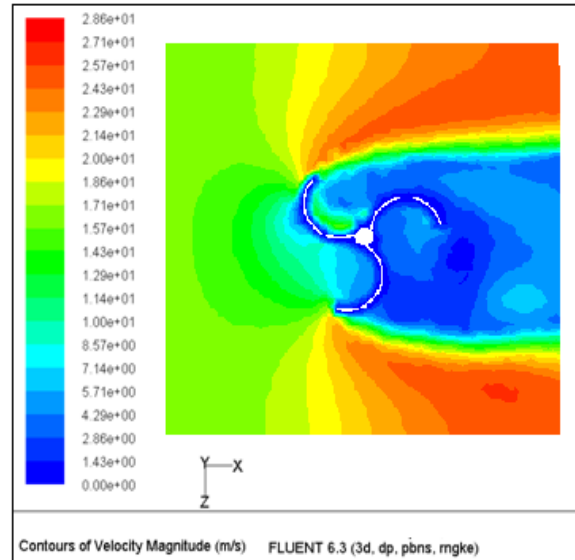**Figure 5 (a): Velocity contour of $0^0$ rotor angle at XZ iso-plane**

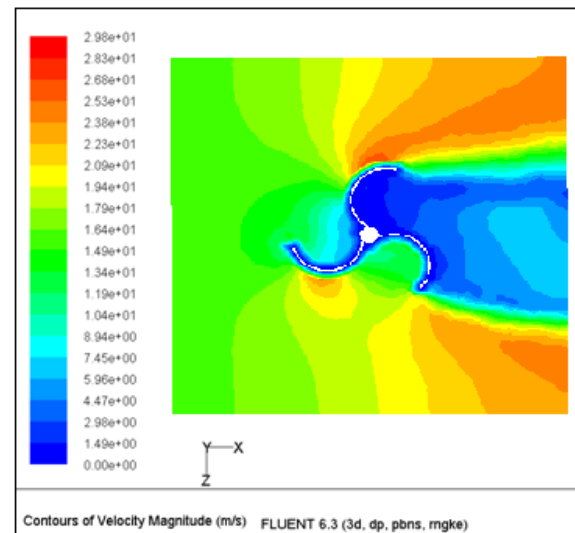**Figure 5 (b): Velocity contour of $60^0$ rotor angle at XZ iso-plane**



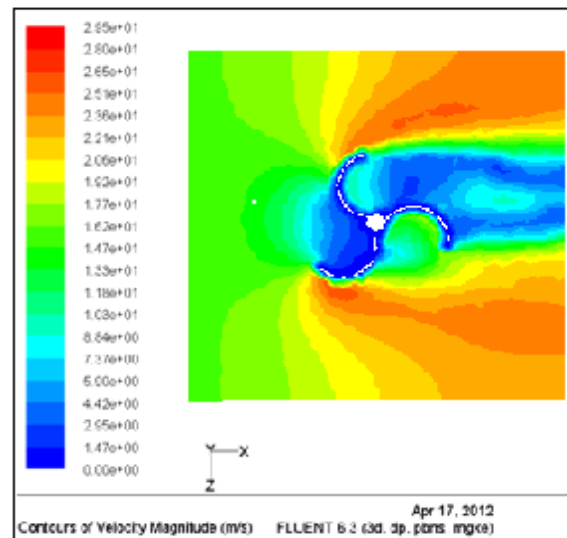**Figure 5 (c): Velocity contour of $120^0$ rotor angle at XZ iso-plane**



**Figure 5 (d): Velocity contour of $150^0$ rotor angle at XZ iso-plane**
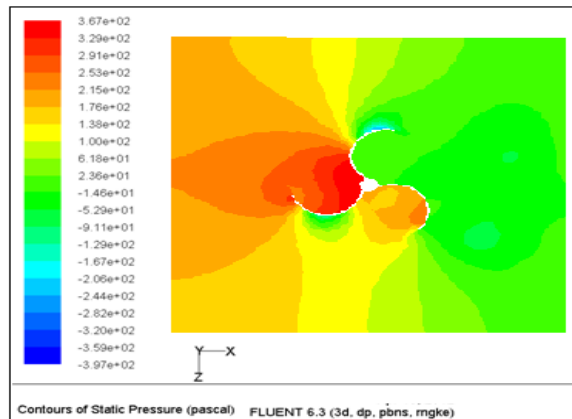
**Figure 6 (a): Static pressure contour of $0^0$ rotor angle at XZ iso-plane**
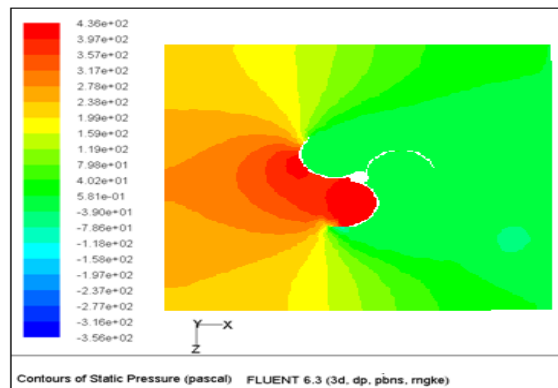


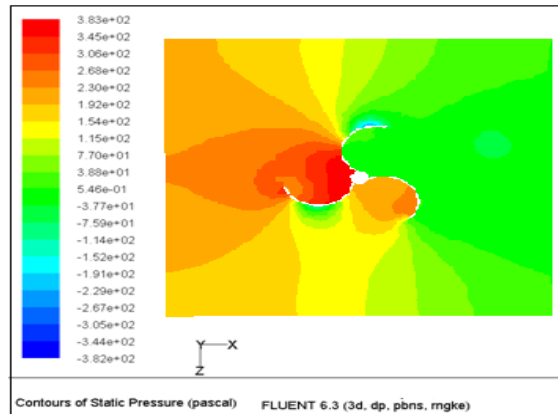**Figure 6 (b): Static pressure contour of $60^0$ rotor angle at XZ iso-plane**



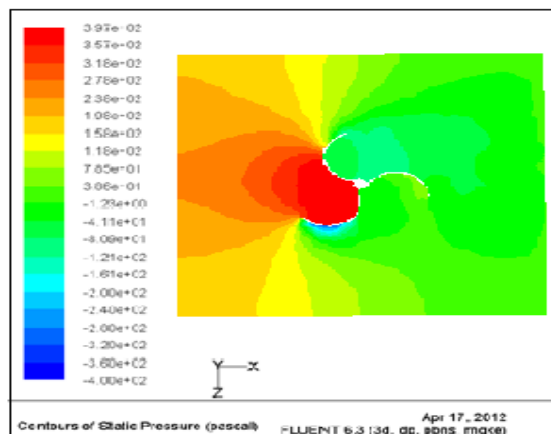**Figure 6 (c): Static pressure contour of $120^0$ rotor angle at XZ iso-plane**



**Figure 6 (d): Static pressure contour of $150^0$ rotor angle at XZ iso-plane**

## VI.  CONCLUSION

Flow physics analysis clearly shows that the static pressure decreases from the upstream side to the downstream side across the rotor, which results in useful lift for the rotor. So the maximum static pressure obtained near to the advanced bucket at $0^0, 60^0, 120^0$ and $150^0$ rotor angle are 367 Pascal, 436 Pascal, 383 Pascal and 397 Pascal. Again for velocity contour analysis the maximum velocity obtained near to the advanced bucket chord at $0^0, 60^0, 120^0$ and $150^0$ rotor angle are 22.3 m/sec, 25.7m/sec, 23.8m/sec and 23.6m/sec. So it can conclude, there is no sharp increase static pressure between rotor angles of $60^0$ to $120^0$. At $60^0$ rotor angle maximum static pressure and velocity magnitude obtained 436 Pascal and 25.7m/sec which is marginally higher compare to other rotor angles, would ensure improved aerodynamic torque of the rotor as a whole during of the power stroke in one revolution of rotor. Flow physics analysis also shows the effect of positive static torque at variation of rotor angle. For 90° twist three buckets helical Savonius rotor at 150° rotor angle maximum positive static pressure distributions near the chord ends is obtained $3.97 \times 10^2$ Pascal to $3.06 \times 10^{-1}$ Pascal from upstream side to downstream side which gives the positive static torque. So it can be concluded from flow physics analysis that three bucket $90^0$ twist angle helical Savonius rotor at $60^0$ rotor angle maximum lift force during power stroke was evaluated and maximum positive static torque was evaluated at $150^0$ rotor angle.

## REFERENCES

[1]   Savonious, S. J., 1931.The Savonius rotor and its applications. Mech Eng. 53(5), pp 333-338.
[2]   N.Fujisawa and F.Gotoh, "Visualization study of the flow in and around a Savonius rotor," Experiments in Fluids, vol. 12, pp 407 412, 1992.
[3]   Nobuyuki Fujisawa,"Velocity measure- ments and numerical calculations of flow fields in and around Savonius rotors," Journal of Wind Engineering and Industrial Aerodynamics, vol. 59, pp 39-50, 1996.
[4]   G. Bergeles and N. Athanassiadis, On the flow field around a Savonius rotor, Wind Eng. 6 (1982) 140-148.
[5]   G.J. Bowden and S.A. McAleese, The properties of isolated and coupled Savonius rotors, Wind Eng. 8 (1984) 271- 288.
[6]   R. Gupta , K.K. Sharma, "Flow Physics of a Three-Bucket Savonius Rotor using Computational Fluid Dynamics (CFD)" International Journal of Research in Mechanical Engineering and Technology, Vol. 1, Issue 1, Oct. 2011.
[7]   R. Gupta, K.K. Sharma, "Flow physics of a combined darrieus-savonius rotor using computational fluid dynamics (CFD)" International Research Journal of Engineering Science, Technology and Innovation Vol. 1(1) pp. 1-13, April, 2012
[8]   M.A. Kamoji, S.B.Kedare and S.V. Prabhu, "Performance tests on helical Savonius rotors," Renewable Energy, vol. 34, pp. 521- 529, 2009.
[9]   Gupta R, Debnath B, Das R. CFD analysis of a two-bucket Savonius rotor using Fluent package. In: Proc. of the European Wind Energy Conference, 2009.
[10]  Gupta R, Biswas A (2011). "CFD Analysis of Flow Physics and Aerodynamic Performance of a Combined Three-bucket Savonius and Three-bladed Darrieus Turbine". Int. J. Green Energy. 8: 209–233.
[11]  Katsuya, I.; Toshio, S. "Simulation of flow around rotating Savonius turbines". Proceedings the sixth National Symposium on Computational Fluid Dynamics, 2001,pp 691-694.
[12]  M.,Manzoor Hussain: Mehdi,S. Nawazish: Reddy, P. Ram: "CFD analysis of low speed vertical axis wind turbine with twisted blades" International Journal of Applied Engineering Research: January,2008: Volume 3: Issue 1.
[13]  Fluent Inc., Fluent Version 6.3 User's guide, Lebanon, New Hampshire, USA; 2006.
[14]  Masson C, Ammara I, Paraschivoiu I (1997). "An aerodynamic method for the analysis of isolated horizontal-axis wind turbines". Int. J. Rotating Mach.vol. 3, pp 21-32.
[15]  FLUENT Inc. "Fluent 6.0 documentation: user's guide" (2005).